Polarons with arbitrary nonlinear electron-phonon interaction

Stefano Ragni [1], Tomislav Miškić [2], Thomas Hahn [3], Nikolay Prokof'ev [4], Osor S. Barišić [2], Naoto Nagaosa [5,6], Cesare Franchini [1,7,*] and Andrey S. Mishchenko [2,5,†]

[1] *Faculty of Physics, Computational Materials Physics, University of Vienna, Kolingasse 14-16, A-1090 Vienna, Austria*
[2] *Department for Research of Materials under Extreme Conditions, Institute of Physics, 10000 Zagreb, Croatia*
[3] *Center for Computational Quantum Physics, Flatiron Institute, 162 5th Avenue, New York, New York 10010, USA*
[4] *Department of Physics, University of Massachusetts, Amherst, Massachusetts 01003, USA*
[5] *RIKEN Center for Emergent Matter Science (CEMS), Wako, Saitama 351-0198, Japan*
[6] *Fundamental Quantum Science Program (FQSP), TRIP Headquarters, RIKEN, Wako 351-0198, Japan*
[7] *Dipartimento di Fisica e Astronomia, Università di Bologna, 40127 Bologna, Italy*

(Received 26 June 2025; accepted 12 November 2025; published 16 December 2025)

We develop an exact computational method based on numerical X propagators for solving polaron models with arbitrary nonlinear couplings of local vibration modes to the electron density and magnitude of the hopping amplitude. Our approach covers various polaron models, some of which were impossible to treat by any existing approximation-free techniques. Moreover, it remains efficient in the most relevant but computationally challenging regime of phonon frequencies much smaller than the electron bandwidth. As a case study, we consider the double-well type nonlinear model with quadratic ($g_2 < 0$) and quartic ($g_4 > 0$) interactions describing a broad class of technologically important materials, such as quantum paraelectric compounds and halide perovskites. We observe, depending on the model parameters, three qualitatively different regimes: (1) quantum interplay of quartic and quadratic interactions that suppresses effects of the quadratic coupling, (2) intermediate-coupling regime with exponential $\propto \exp(\alpha g_2 \Omega^{-1/4})$ scaling of the quasiparticle weight and mass renormalization, and (3) strong-coupling asymptotic behavior.

DOI: 10.1103/6127-phps

I. INTRODUCTION

The vast majority of the polaron literature considers linear coupling between electrons and displacements, $\{x_i\}$, of lattice ions [1–4]. However, it was recently realized that there exist many cases where lattice displacements in response to the electron density on site i, $V_{\rm ep}(x_i)$, and/or hopping between sites i and j, $t(x_i, x_j)$, are better described by nonlinear functions $V_{\rm ep}(x)$ and $t(x, x')$: halide perovskites [5–7], doped manganites [8,9], quantum paraelectrics [10–13], and common crystal structures consisting of intercalated sublattices of heavy and light atoms [14,15]. The superconducting pairing mechanism based on the two-phonon exchange process originally suggested in Ref. [16] was revisited recently to explain T_c properties in $SrTiO_3$ [17,18]. A generic nonlinear coupling $V_{\rm ep}(x)$ involves quadratic x^2 and higher order in x dependencies, leading, e.g., to the double-well potential for ions in quantum paraelectrics and ferroelectrics [14,15,19–22]. Finally, material physics applications may require accurate treatment of generic nonlinear electron-phonon interaction (EPI) when the function $V_{\rm ep}(x)$ is a numerical result originating from first-principles calculations [23,24].

Several studies devoted to the nonlinear electron-lattice interaction were either based on various approximations or limited to the weak-coupling regime: these include Refs. [14,15,25] employing the momentum average (MA) approximation [26–28], variational solutions [29], quantum [30] and determinant [31–33] Monte Carlo calculations restricted to finite clusters, and perturbation theory treatment [34]. Recently, an extended Fröhlich polaron model incorporating quadratic EPI was studied in Refs. [35,36] using the variational Feynman's path integral [37] and other analytic methods.

However, approximations can be detrimental already in the well-characterized case of linear interactions, where moderate-to-strong coupling results in the breakdown of the quasiparticle picture because of the Mott-Ioffe-Regel limit violation [38,39]. Approximate treatments of nonlinear EPI are even more doubtful because they can, in contrast to the well-conditioned case of linear EPI, cause system instability even for single polarons [40]. Therefore, an exact method capable of treating polarons with arbitrary nonlinear EPI is highly desirable for achieving a precise theoretical understanding of the system and its technological applications. Significant progress toward this goal was made recently by developing the diagrammatic Monte Carlo (DMC) method in momentum representation for quadratic coupling [40], and

*Contact author: cesare.franchini@univie.ac.at
†Contact author: andrey.mishchenko6363@gmail.com

Published by the American Physical Society under the terms of the Creative Commons Attribution 4.0 International license. Further distribution of this work must maintain attribution to the author(s) and the published article's title, journal citation, and DOI.

by combining the path-integral DMC with the X representation of vibrational modes [40,41], which established an approximation-free framework for dealing with linear and quadratic EPI. However, the key element in the last approach, namely, an exact analytic expression for phonon propagators in the X representation, is not available for arbitrary EPI potentials. To proceed with a precise treatment of generic first-principles EPI coupling profiles, e.g., double-well potentials important for understanding anomalous properties of polarons in ferroelectric and quantum paraelectric materials [42,43], one needs to overcome this crucial shortcoming.

In this work, we develop a numerical X-propagator (NXP) method suitable for studying arbitrary nonlinear coupling to local lattice displacements. After we describe the computational technique for a general form of coupling, we apply it to the double-well potential, a system of broad relevance and interest, particularly for anharmonic materials that have been the focus of recent studies [13,20–22,44–46]. We show how exact and approximate treatments deviate from each other in the adiabatic limit, where the phonon frequency is sufficiently small compared to the bare electronic hopping rate, which is the most relevant parameter regime for real materials.

The manuscript is organized as follows: Section II defines the model (Sec. II A) and methods, with Sec. II B outlining the role of X propagators in the technique, and Sec. II C describing the tabulation methodology for arbitrary electron-lattice potentials. Section III contains results on the ground-state properties of the double-well model for two different sets of parameters in Secs. III A and III B, respectively. Section III C contains an analysis of excited states and spectral properties. We present our conclusions and outlook in Sec. IV.

II. MODEL AND METHOD

The general Hamiltonian, which can be treated by the method developed in this paper, is

$$\widehat{H} = \sum_{\langle ij \rangle} -t_{ij}(x_i, x_j)\, c_i^\dagger c_j + \sum_i \widehat{H}^{(\mathrm{i})}_{\mathrm{e-p}}(x_i), \tag{1}$$

where $c_i^\dagger$ (c_i) is the creation (annihilation) operator of an electron on site i and $t_{ij}(x_i, x_j)$ is the hopping amplitude between sites i and j, which depends on the local vibrational coordinates x_i and x_j, respectively. We assume that $t_{ij}(x_i, x_j) > 0$ for any (x_i, x_j); i.e., lattice vibrations do not change the hopping sign. The second term, $\widehat{H}^{(\mathrm{i})}_{\mathrm{e-p}}(x_i)$, is the on-site Hamiltonian, which consists of the harmonic term describing atomic vibration with frequency Ω in the absence of the electron and an additional arbitrary potential $V_{\mathrm{ep}}(x_i)$ present only when the electron occupies the site i:

$$\widehat{H}^{(\mathrm{i})}_{\mathrm{e-p}}(x_i) = \Omega b_i^\dagger b_i + n_i \sum_{n=1}^{\infty} g_n (b_i^\dagger + b_i)^n, \tag{2}$$

where $b_i^\dagger$ (b_i) is the creation (annihilation) operator of a local vibration mode with frequency Ω on site i [we count harmonic oscillator (HO)energies from $\Omega/2$] and expansion coefficients g_n reproduce the potential $V_{\mathrm{ep}}(x_i)$. This term effects atomic vibrations only when the electron occupation number on site i, $n_i = c_i^\dagger c_i$, is nonzero. To keep the connection with the standard form of the Hamiltonian (1) in terms of the physical displacement coordinate $x_i = (b_i^\dagger + b_i)/\sqrt{2\Omega}$ (the oscillator mass m and Planck constant $\hbar$ are set to unity), the same Hamiltonian can be written as

$$\widehat{H}^{(\mathrm{i})}_{\mathrm{e-p}}(x_i) = -\frac{1}{2}\frac{\partial^2}{\partial x_i^2} + V(x_i) \tag{3}$$

with potential

$$V(x_i) = \frac{\Omega^2}{2} x_i^2 + n_i V_{\mathrm{ep}}(x_i) \tag{4}$$

being the sum of the harmonic and electron density dependent terms. Consistency with Eq. (2) implies

$$V_{\mathrm{ep}}(x) = \sum_{n=1}^{\infty} g_n (2\Omega)^{n/2} x^n. \tag{5}$$

This Hamiltonian covers many existing polaron models. For example, a displacement-independent first term and a linear $V_{\mathrm{ep}}(x_i)$ are known as the Holstein model. On the other hand, a displacement dependent $t_{ij}(x_i, x_j)$ and $V_{\mathrm{ep}} = 0$ lead to the Barišić-Labbe-Friedel-Su-Schrieffer-Heeger (BLF-SSH) model [47–50]. Both Holstein [28,51,52] and BLF-SSH [53,54] systems are solvable numerically by several techniques, especially in one dimension and for large values of the Ω/t ratio in the antiadiabatic regime.

However, to treat linear plus quadratic dependence of $V(x_i)$, the adiabatic regime ($\Omega/t \ll 1$), higher-dimensional lattices, and arbitrary dependence of the hopping magnitude $t_{ij}(x_i, x_j)$ on lattice vibrations, the only approximation-free approach is the X-representation DMC method of Refs. [40,41]. In this approach, the electron path-integral is "dressed" by propagators of displaced vibrational modes in imaginary time (X propagators):

$$U(x_i(\tau_1), x_i(\tau_2), \tau) = \langle x_i(\tau_1)|\, e^{-(\tau_2-\tau_1)\widehat{H}^{(\mathrm{i})}_{\mathrm{e-p}}(x_i)}\, |x_i(\tau_2)\rangle\,, \tag{6}$$

where $\tau = \tau_2 - \tau_1$. Previous studies were limited to the linear plus quadratic dependence of $V(x_i)$ because only in this case there exists an analytic expression for U.

In the present work, we develop an NXP method that can be used for exact treatment of any potential $V(x_i)$ in the Hamiltonian (1), which, thus, makes this Hamiltonian exactly solvable for any form of the electron-phonon interaction. In particular, we study the case of the double-well potential, which is considered a property governing physical processes in several technologically critical correlated materials [5,10,14,19,23]. Moreover, the double-well potential is considered to be a general property of materials showing Jahn-Teller distortions [55].

A. Model

The minimal EPI model featuring the local double-well potential can be formulated as Eq. (2), where the EPI term has nonzero coupling constants only for quadratic, $g_2 < 0$, and quartic, $g_4 > 0$, powers of x. Hopping amplitudes t in the one-dimensional (1D) lattice are nonzero only for nearest neighbors and are independent of local vibrational coordinates x. We restrict our study to the one-dimensional case because of the weak dependence of the polaron properties on dimensionality for nonlinear coupling [40].

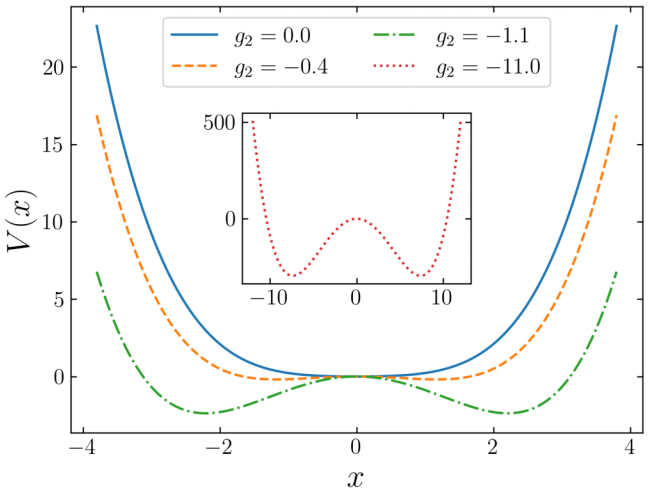

FIG. 1. Potential energy profiles described by Eq. (4) when only g_2 and g_4 are nonzero in $V_{\rm ep}(x)$. $g_4 = 0.1$ and $\Omega = 0.5$ are kept fixed and four values of g_2 are shown, representative of different physical regimes that will be probed in the remainder of the text.

The properties of the model are defined by three independent dimensionless parameters (taking hopping t as the unit of energy); see Eqs. (1) and (2): adiabatic ratio Ω/t, g_2/t, and g_4/t. Since there is no particularly insightful way to define a single effective coupling, we chose to work with the bare coupling constant similar to Ref. [14]. Qualitative behavior for different values of g_4 was already studied in Ref. [14]; therefore, we focus on the g_2-dependence for different Ω/t ratios all the way to the adiabatic limit $\Omega/t \ll 1$.

A minimal graphical representation of the potential is shown in Fig. 1. For $g_2 = 0$, the potential is single well. When $g_2 < -\Omega/4$, the lattice becomes unstable. In this regime, the inclusion of anharmonic (quartic) terms stabilizes the system and gives rise to the characteristic double-well shape of the potential with two minima located at

$$x_0 = \pm\sqrt{\frac{-4g_2 - \Omega}{16g_4\Omega}} \tag{7}$$

with the equilibrium potential energy

$$E_\pm = -\frac{(4g_2/\Omega + 1)^2\Omega^2}{64g_4}. \tag{8}$$

The oscillator frequency at the minima is

$$\tilde{\omega} = R\Omega, \tag{9}$$

where

$$R = \sqrt{2(-4g_2/\Omega - 1)}. \tag{10}$$

As shown in Fig. 1, decreasing g_2 leads to a higher energy barrier and a greater spatial separation between the two minima. The single-well ($g_2 = 0$) and shallow double-well ($g_2 = -0.4$) potentials are a defining feature of (quantum) paraelectrics. At the same time, deeper and more separated wells are typical of a ferroelectric material, such as $BaTiO_3$ below its Curie temperature [20,43].

Strictly speaking, there is no consensus on how the interaction potential and its strength change with doping in ferroelectric and quantum paraelectric materials such as $BaTiO_3$, $SrTiO_3$, and $KTaO_3$. Some theoretical approaches assume $g_2 > 0$ [11,18]. However, these studies evidently neglect quartic $\sim g_4 > 0$ terms in the considered materials, and one cannot be certain that this assumption does not result from the cumulative effect of higher-order terms of the electron-phonon potential, which are neglected in the theoretical treatment.

We are not aware of any theoretical results regarding the doping dependence of the double-well potential, although experimental data suggest possible trends. The phonon frequency increases with doping, indicating that either g_2 or g_4 changes when an electron is present at a given site [56]. Specifically, this behavior can be caused either by decreasing the absolute value of the negative quadratic coefficient g_2 or by increasing the positive quartic order constant g_4. Noting the simultaneous increase in the frequency and linewidth of the Raman signal, an increase in g_4 is more plausible because it introduces additional anharmonicity, which causes the notable increase in linewidth [56].

This implies that the real situation in $BaTiO_3$, $SrTiO_3$, and $KTaO_3$ can be described by a model where two different double-well electron-phonon potentials are associated with the sites with and without the added electron, resulting from the unknown, though definitely nonlinear, shape of the electron-phonon potential. Our method is applicable to any shape of the potential of the empty state and any displacement dependence of the electron-phonon coupling thanks to our robust tabulation of X propagators. We note that the double-well shape of the electron-phonon potential is not limited to quantum paraelectric and superconducting materials; rather, it is a general feature of many materials exhibiting manifestations of the Jahn-Teller effect [55]. Here, instability due to linear electron-phonon coupling leads to a double-well structure, resulting in large displacements and, consequently, nonlinear effects.

Actually, our method does not require division into bare electron potential and electron-phonon coupling, which is often an ill-defined task that cannot be performed without the treatment of the vibrational problem from bare ions coupled by Coulomb interaction [57] because of an erroneous account of nonadiabatic corrections [58] or Fermi blockade of electron-phonon coupling at finite dopings [59]. It is clear from Eqs. (3)–(4) that for tabulation of all necessary X propagators, it is enough to know the potential profile $V(x_i)$ for empty and filled states, making our method a robust tool for treatment of realistic materials based on first principles band structure calculations.

However, there is yet no precise knowledge of how the potential changes when an electron is added at a site. Therefore, instead of pursuing a description of the unknown parameters of quantum paraelectrics, we concentrate on benchmarking our results against previous studies [14,15,25]. Namely, we consider the case of no electron-phonon potential in the empty site and potential in Fig. 1 with $g_2 < 0$ and $g_4 > 0$ for the filled site.

B. X representation

The X-representation technique aims at computing the imaginary-time (Matsubara) Green's function [41]

$$G_r(\tau > 0) = \langle c_r(\tau) c_0^\dagger \rangle. \tag{11}$$

The Hamiltonian in Eq. (1) is split into the diagonal (with respect to the electron occupation number) part

$$\hat{H}_0 = \sum_i \widehat{H}^{(\mathrm{i})}_{\mathrm{e-p}}(x_i), \tag{12}$$

and off-diagonal (hopping) part

$$\hat{T} = \sum_{\langle ij \rangle} -t_{ij}(x_i, x_j)\, c_i^\dagger c_j. \tag{13}$$

Similar to direct space DMC [60,61], one then carries out a perturbative expansion in powers of the electron hopping, considered formally as a Taylor series expansion of the so-called $\mathcal{T}$-exponent:

$$G_r(\tau > 0) = \langle c_r(\tau) S(\tau) c_0^\dagger \rangle_0, \tag{14}$$

$$S(\tau) = \mathcal{T} \exp\left(- \int_0^\tau \mathrm{d}\tau'\, \hat{T}(\tau') \right). \tag{15}$$

The zeroth-order term yields the atomic limit (AL) Green's function

$$G_r^0(\tau) = \delta_{r0} \langle e^{\tau \hat{H}_0} c_r e^{-\tau \hat{H}_0} c_0^\dagger \rangle_0. \tag{16}$$

To represent the many-body state, we consider the following basis: $|r, \{x_i\}\rangle$, where $|r\rangle$ is an electronic orbital localized on site r and $|x_i\rangle$ is an oscillator state on site i with displacement x_i. Since we study a single electron in an otherwise empty band at temperature $T = 1/\beta$, the average in Eq. (16) is done with respect to the thermodynamic state of all harmonic modes when $\{n_i = 0\}$; we denote it as $|\varnothing\rangle$. In this basis

$$G_r^0(\tau) = \int \mathrm{d}x_0(0) \times \langle \varnothing, x_0(0)|\, e^{-(\beta-\tau)\hat{H}_0} c_r e^{-\tau \hat{H}_0} c_0^\dagger\, |\varnothing, x_0(0)\rangle \tag{17}$$

$$= \int \mathrm{d}x_0(0) \int \mathrm{d}x_0(\tau) \times U(x_0(0), x_0(\tau), \beta - \tau) \tilde{U}(x_0(\tau), x_0(0), \tau), \tag{18}$$

where we have inserted a complete set of vibrational basis states on site 0, $\int \mathrm{d}x_0(\tau)\, |0, x_0(\tau)\rangle\, \langle 0, x_0(\tau)|$. The U propagators on all empty sites can be ignored, because they reduce to partition function factors that cancel between the numerator and denominator in the average, or, equivalently, their integrated contribution is unity in the $T = 0$ case considered in this work. Propagators U and $\tilde{U}$ correspond to different local Hamiltonians, depending on the absence or presence of the electron on a given site, respectively. Lastly, we include an electronic part containing an artificial "chemical potential" μ,

$$G_{\mathrm{el}}(\tau) = e^{\mu \tau}, \tag{19}$$

to control the asymptotic decay of the solution in numerical simulations.

At first order, one hopping event occurs at time $\tau_1 < \tau$. Initially placed on site $i = 0$, the electron hops to one of the nearest-neighbor sites, say to site $i = 1$. We repeat the procedure of inserting a complete set of vibrational states on site $i = 1$ to arrive at

$$\int_0^\tau \mathrm{d}\tau_1 \int \mathrm{d}x_0(0) \int \mathrm{d}x_0(\tau_1) \int \mathrm{d}x_1(\tau_1) \int \mathrm{d}x_1(\tau) \times U(x_1(\tau_1), x_1(\tau), \beta - \tau + \tau_1)\, \tilde{U}(x_1(\tau), x_1(\tau_1), \tau - \tau_1)\, \tilde{U}(x_0(\tau_1), x_0(0), \tau_1)\, U(x_0(0), x_0(\tau_1), \beta - \tau_1)\, t_{10}(x_1(\tau_1), x_0(\tau_1)) \times G_{\mathrm{el}}(\tau). \tag{20}$$

In Eqs. (18)–(20), we have cast the Green's function order-by-order contributions as products of elementary propagators, integrated over the basis states, which is reminiscent of the usual Feynman diagram representation.

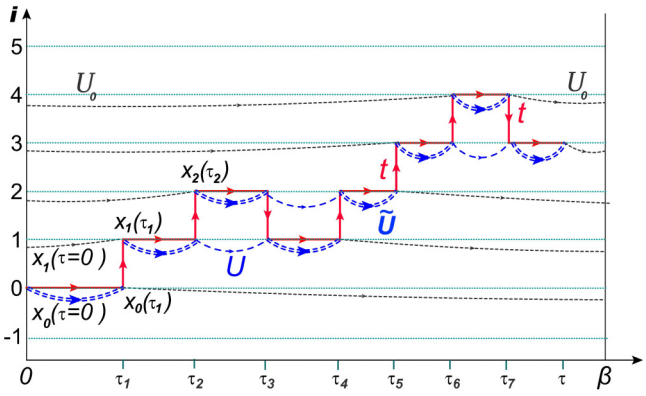

FIG. 2. (Modified from supplement in Ref. [40]) Green's function (14) diagrams in one-dimensional space (index i) and imaginary time (τ) plane. Horizontal solid red lines with arrows are bare Green's functions (19), while vertical lines with arrows are hopping events t. $\tilde{U}$ (double-line dashed arcs with arrows) and U (single-line dashed arcs with arrows) are X propagators with and without the electron on a given site, respectively. U_0 (dotted lines with arrows) is the limiting value of the X propagator in the ground-state technique (A5).

A generic high-order expansion term is illustrated in Fig. 2. Detailed expressions and methods of calculating U and $\tilde{U}$ propagators are discussed in Sec. II C and Appendix A. At $\beta \to \infty$, the X propagators connected to the leftmost and rightmost parts of the electron path transform into their limiting ground-state form U_0; see Appendix A. Each expansion term can be considered as a diagram with a well-defined mathematical weight given by a product of G_{el}, t_{ij}, U_0, U, and $\tilde{U}$ diagram elements. Diagrams can then be generated algorithmically by a Monte Carlo process using updates that add and remove hopping events and integrate over the displacement variables $x_0, x_1, \ldots, x_\tau$, and imaginary times $\tau_1, \tau_2, \ldots, \tau$ (see Fig. 2) [40].

C. X propagators for an arbitrary interaction potential

Previous applications of the X-representation technique [40,41] were limited to potentials with linear and quadratic terms that simply change the local Hamiltonian from one harmonic form to another and, thus, admit an analytic solution for $\tilde{U}$ (see Appendix A 1). This limitation can be removed by

precise tabulation of $\tilde{U}$ for an arbitrary potential. We propose two distinct methods for the numerical computation of $\tilde{U}$.

The first method is based on the Trotter-Suzuki decomposition [62,63], to simulate the path-integral of the vibrational coordinate [64]:

$$\tilde{U}(x_f, x_i, \tau) = \int dx_1 dx_2 \ldots dx_{N-1} \langle x_f(\tau_f)| e^{-\hat{H}^{(i)}_{e-p}\delta\tau} \times |x(\tau_{N-1})\rangle \ldots \langle x(\tau_1)| e^{-\hat{H}^{(i)}_{e-p}\delta\tau} |x(\tau_i)\rangle ,$$

where the τ interval is divided into N short time slices $\delta\tau = \tau/N$, which allows decomposition of kinetic and potential energy and results in the following representation:

$$\tilde{U}(x_f, x_i, \tau) = \int dx_1 dx_2 \ldots dx_{N-1} P(x_f, x_{N-1}, \delta\tau) \ldots \times P(x_2, x_1, \delta\tau) P(x_1, x_i, \delta\tau),$$

where

$$P(x, x', \delta\tau) = \frac{1}{\sqrt{2\pi\delta\tau}} \exp\left\{-\delta\tau\left[\frac{(x-x')^2}{2\delta\tau^2} + \frac{V(x)+V(x')}{2}\right]\right\} \tag{21}$$

is the free particle propagator in the presence of the (symmetrized) potential $[V(x)+V(x')]/2$. One may significantly improve the efficiency of simulations by replacing $P(x, x', \delta\tau)$ with the exact harmonic oscillator solution [similar to $U(x, x', \delta\tau)$] for the potential $V(\bar{x}) + V'(\bar{x})(x-\bar{x}) + V''(\bar{x})(x-\bar{x})^2/2$, where $\bar{x} = (x+x')/2$.

The Monte Carlo simulation of $\tilde{U}$ is then performed on the time mesh $\tau(i) = i\,\delta\tau$, up to some large imaginary time $\tau_{\max}$, by sampling all possible values of x coordinates on all time slices. The simplest set of updates for an arbitrary $V_{ep}(x)$ is presented in Appendix A 2. The coordinates of the initial and final time slices are measured to collect statistics of $\tilde{U}$. In practice, after introducing the coordinate mesh $x_j = dx(j-1/2)$, we collect statistics to bins of size dx. Let the corresponding histogram bin representing propagation from bin j to bin k in time τ_n be $S(j, k, n)$. The normalization is achieved by collecting statistics for $S(0, 0, \delta\tau)$, which is also known extremely accurately analytically because at $x = 0$, the quartic terms can be neglected. Thus, if

$$\mathcal{M} = \int_{-dx/2}^{dx/2} dx \int_{-dx/2}^{dx/2} dx' P(x, x', \delta\tau), \tag{22}$$

then, the properly normalized statistics for $\tilde{U}$ reads

$$\tilde{U}(x_j, x_k, \tau_n) = \mathcal{M}\frac{S(j, k, n)}{S(0, 0, 1)}\frac{1}{dx^2}. \tag{23}$$

Since we can afford to store rather dense meshes in memory, to incorporate numeric X propagator to the DMC technique described in Sec. II B, we employ three linear space-time interpolations to get $\tilde{U}$ for $\tau > \delta\tau$, and

$$\mathcal{U}(x, x', \tau) = P(x, x', \tau) \tag{24}$$

for $\tau < \delta\tau$.

The second method to numerically tabulate the X propagator is the single-site exact diagonalization (SSED) approach presented in Appendix B. For the double-well potential studied in this work, it is more accurate and efficient than the general Monte Carlo approach. We benchmarked the two methods by comparing with analytic solutions for linear and quadratic cases, and cross validated them by comparing results for the double-well potential. The only minor limitation of the exact diagonalization approach for a generic case is that it requires explicit expansion of the interaction potential into a series (5) and may become less effective when the necessary expansion order is large. The SSED, used for calculating the X propagator, mitigates the Hilbert space truncation that typically occurs when applying exact diagonalization to the entire lattice. The remainder of the article uses the term "exact diagonalization" (ED) to refer to the approximate method of solving the problem of a polaron in the lattice with truncated Hilbert space.

In particular, in our ED calculations, we use a subspace of approximately 18 million translationally invariant states [51,65]. These states correspond to different configurations of phonon excitations with respect to the electron. The subspace is constructed by joining two different sets of states. The first involves up to 2^{16} states at the occupied site. The second one involves all the states obtained by acting the interaction Hamiltonian (1) on the zero-phonon state up to 14 times.

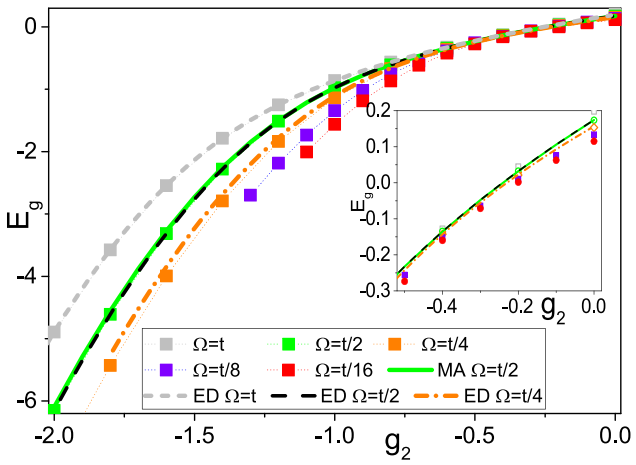

FIG. 3. Energy renormalization for $t = 1$, $g_4 = 0.1$ as a function of g_2 for different values of Ω. Points are our numeric data. Error bars, if not shown, are smaller than the symbol size. Momentum average (MA) method data [14] for $\Omega = t/2$ are shown by the green solid line, and ED method data for $\Omega = t$, $\Omega = t/2$, and $\Omega = t/4$ are shown by the gray dashed, black dashed, and orange dash-dotted lines, respectively. Dotted lines between the points of our numeric data are meant to guide the eye.

III. RESULTS

A. Ground-state properties at fixed t and g_4

This subsection presents results obtained by fixing the value of $g_4/t = 0.1$ and exploring ground-state properties as a function of g_2/t for different values of $\Omega = t, t/2, t/4, t/8, t/16$. In Fig. 3, we plot polaron energy counted from the bottom of the one-dimensional band at $-2t$ (when all interaction parameters are set to zero). The

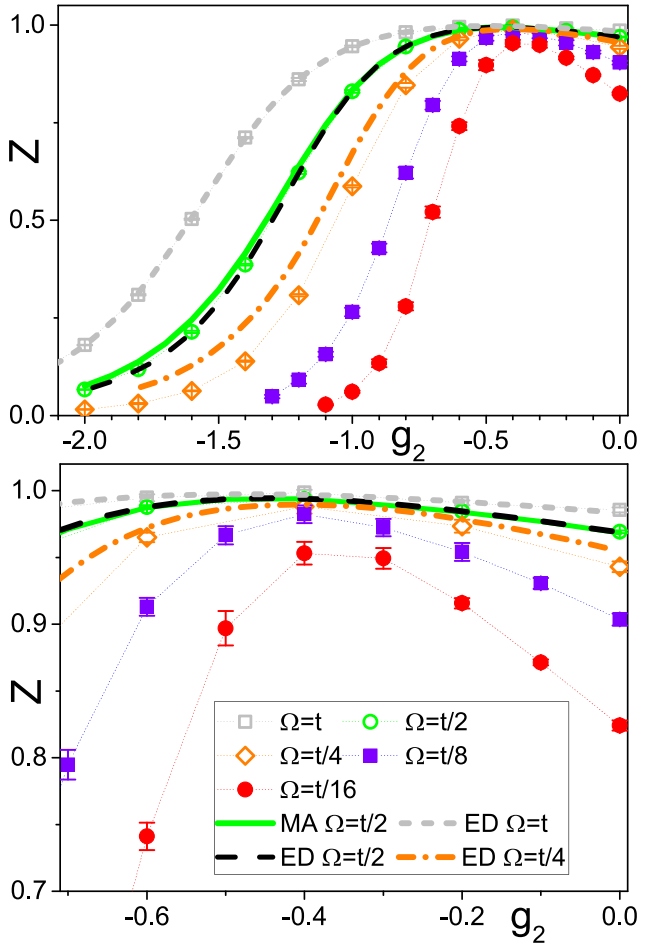

FIG. 4. Quasiparticle weight Z. For notations, see the Fig. 3 caption. Upper panel data are shown over a broad range of g_2/t variation. Lower panel is focusing on the small g_2 region.

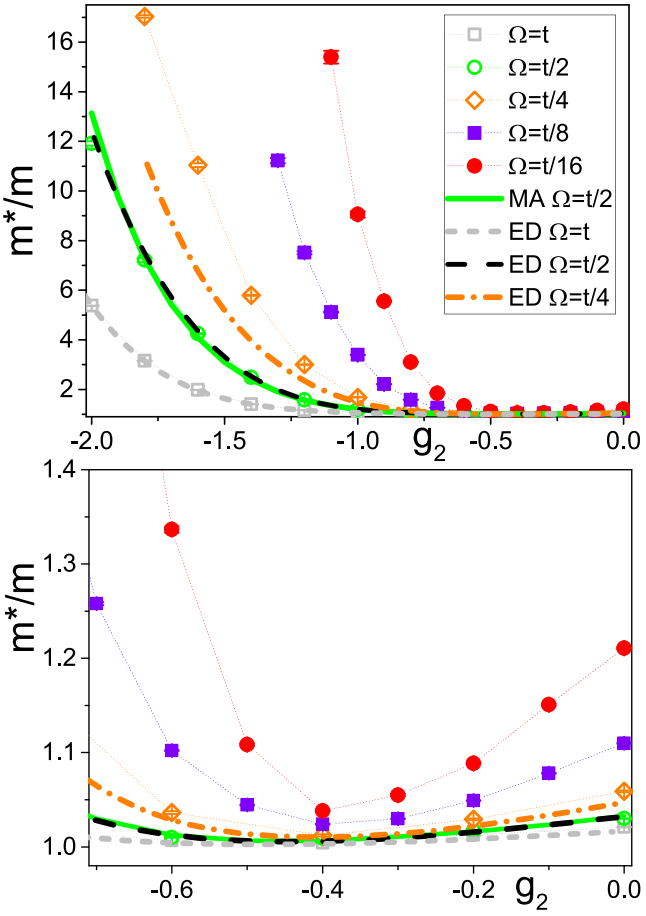

FIG. 5. Effective mass renormalization m^*/m. For notations, see the caption of Fig. 3. Upper panel data are shown over a broad range of g_2/t variation. Lower panel is focusing on the small g_2 region.

quasiparticle weight Z is shown in Fig. 4, and Fig. 5 presents data for the effective mass renormalization, m^*/m, where $m = 1/(2t)$ is the bare mass. We note that for negative $g_2 \approx -0.4$ there is destructive "interference" between the quadratic and quartic interactions. This leads to the effective suppression of the total EPI strength, resulting in $Z \approx 1$ and $m^*/m \approx 1$. Note, the smaller the phonon frequency, the more prominent the nonmonotonicity of the data. This is in line with the properties of linear electron-phonon interaction, showing sharper crossover from the weak to strong coupling regime at lower frequencies [66,67], which leads to abrupt transitions in fully adiabatic models [68].

ED and MA methods provide accurate benchmarks for cases with relatively large phonon frequency Ω where they work best. This is no longer the case in the adiabatic regime due to known limitations of existing techniques, and for $\Omega \leqslant t/4$ we clearly observe large differences in results, especially for the Z factor and effective mass.

We start by comparing our approximation-free data with results of the pioneering MA study [14,15,25] at $\Omega = t/2$ shown by the solid green lines in Figs. 3–5. We find excellent agreement for the polaron energy (see Fig. 3), and the first impression is that there is also good agreement for the quasiparticle weight (Fig. 4) and mass renormalization (Fig. 5), but differences may be hidden in the strong dependence of these quantities on g_2. Larger discrepancy for Z and m^*/m is expected because the MA technique applied to the double-well model [14,15,25] obtains a local self-energy and predicts that

$$Z(m^*/m) \equiv 1. \tag{25}$$

It is clear from Fig. 6 that $Z(m^*/m)$ deviates from unity significantly in the strong coupling regime for all values of Ω/t. This is quite remarkable, since in the 1D linear Holstein model, although the self-energy is nonlocal [69], the deviation from locality is small [70]. A nonlocal self-energy may still be obtained within MA by using a more elaborate, improved variant [27,53,71] over the one utilized in Ref. [14].

Next, we compare our results with ED calculations [51,65], which do not assume locality of the self-energy but rely instead on a truncation of the Hilbert space. We find perfect agreement for all calculated properties at $\Omega = t$ (dotted gray lines in Figs. 3–5), including the $Z(m^*/m)$ product(see Fig. 6). At $\Omega = t/2$, the energy, Z factor, and effective mass data are also in good agreement with ED calculations (dashed black lines in Figs. 3–5), but systematic bias coming from the Hilbert space truncation becomes visible for $Z(m^*/m)$

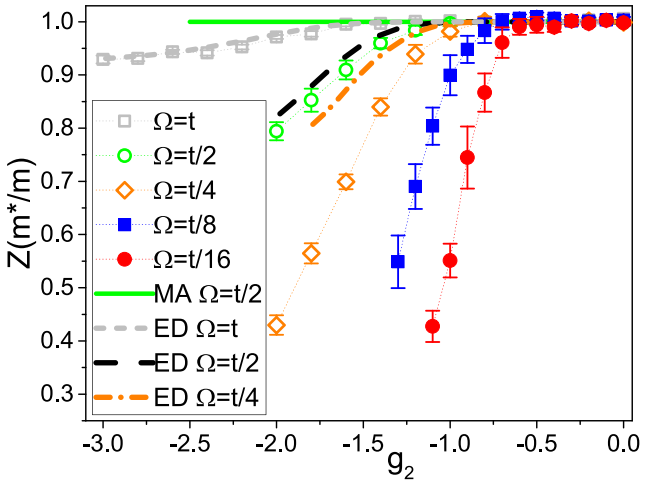

FIG. 6. $Z(m^*/m)$ product as a function of g_2/t. For notations, see the caption of Fig. 3.

(Fig. 6). Finally, for $\Omega = t/4$, all properties computed by the ED method (dash-dot orange lines) deviate from our results significantly. This discrepancy originates from the necessity to keep a large but finite number of basis states in ED calculations. As the adiabatic limit (soft lattice vibrations) is approached, the number of relevant basis states grows too rapidly for the ED method to remain computationally feasible.

It is expected that in the strong coupling limit both Z and m^* are exponential functions of g_2 as a direct consequence of the exponentially vanishing overlap between the vibrational state corresponding to empty and occupied sites. This expectation is confirmed by Fig. 7, where exponential dependence on g_2 is observed for all values of Ω. More precisely, all data for Z can be fit to $f_z = \exp[\xi_Z g_2 \Omega^{-1/4}]$, and all data for m^*/m can be fit to $f_z = \exp[-\xi_m g_2 \Omega^{-1/4}]$, with Ω-independent $\xi_Z = 3.0$ and $\xi_m = 2.6$. The scaling with frequency Ω is surprising and cannot be reproduced by simple considerations. Note, these exponential laws are approximately valid for more than an order of magnitude variation in frequency: $1/16 \leqslant \Omega \leqslant 1$.

B. Ground-state properties at different hopping

In this subsection, we explore how system properties evolve when we change the hopping amplitude. In the previous section, we used t as the unit of energy and worked with the parameter set t, Ω, g_2, g_4 with fixed g_4. If we change hopping by a factor of γ (in this subsection, we consider $\gamma = 1, 2, 4$), while keeping the phonon frequency and quartic coupling fixed, we will study a model with parameter set

$$\{\gamma t, \bar{\Omega}, \bar{g}_2, \bar{g}_4\}_{\bar{g}_2,\gamma}. \tag{26}$$

Since the choice of the energy unit is arbitrary, we can equivalently consider the set

$$\left\{t, \Omega = \frac{\bar{\Omega}}{\gamma}, g_2 = \frac{\bar{g}_2}{\gamma}, g_4 = \frac{\bar{g}_4}{\gamma}\right\}_{g_2,\gamma}.$$

In what follows, we fix $\bar{\Omega} = t/2$ and $\bar{g}_4 = t/10$. The reason for considering this parameter scaling is to compare all curves to the unique single-site limit (see Fig. 8), since, at each g_2, all parameters of the local Hamiltonian (2) are kept fixed.

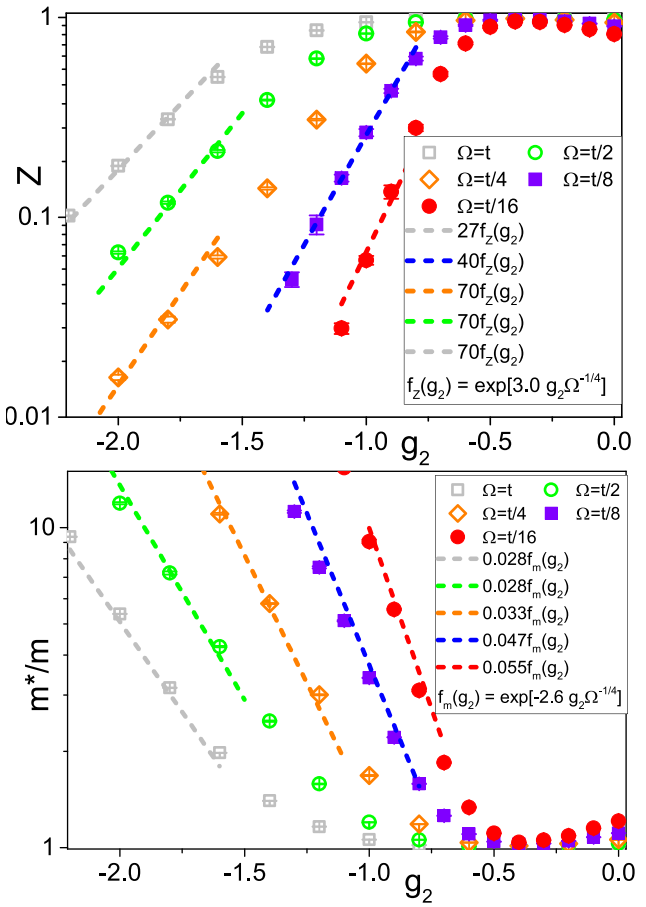

FIG. 7. Universal exponential scaling of the quasiparticle weight and effective mass in the intermediate g_2 region; see text and figure legend. Notations are identical to those in Fig. 3.

It is well known that for linear EPI (no matter whether the coupling is to optical [66] or acoustic [67] modes) the crossover to the strong coupling regime at $\lambda = g_1^2/(2t\Omega) \sim 1$ is sharper for smaller Ω/t. We observe a similar trend (see Fig. 8), but the effect is much less pronounced.

The other difference from the linear case is how quickly the strong coupling case is adequately described by the asymptotic AL, $g_2 \ll -1$, when the anharmonic potential can be approximated by two degenerate harmonic wells at local vibrational coordinates $\pm x_0$ (7) and atomic wavefunctions, by a superposition of two shifted Gaussians. In this limit (see Appendix D),

$$Z_0(t=0) = 2 \times \frac{2\sqrt{R}}{1+R} \exp\left(-\frac{R}{1+R} z_0^2\right), \tag{27}$$

where

$$z_0^2 = x_0^2 \Omega = \frac{-4g_2 - \omega}{16 g_4}, \tag{28}$$

and R is given by Eq. (10). As one can see in Fig. 8, our data are still far from the single-site asymptotic behavior despite Z and m^* changing by nearly two orders of magnitude. (Comparison with SSED result in this limit shows that the asymptotic behavior is reached only at $|g_2| > 5$; see Fig. 11).

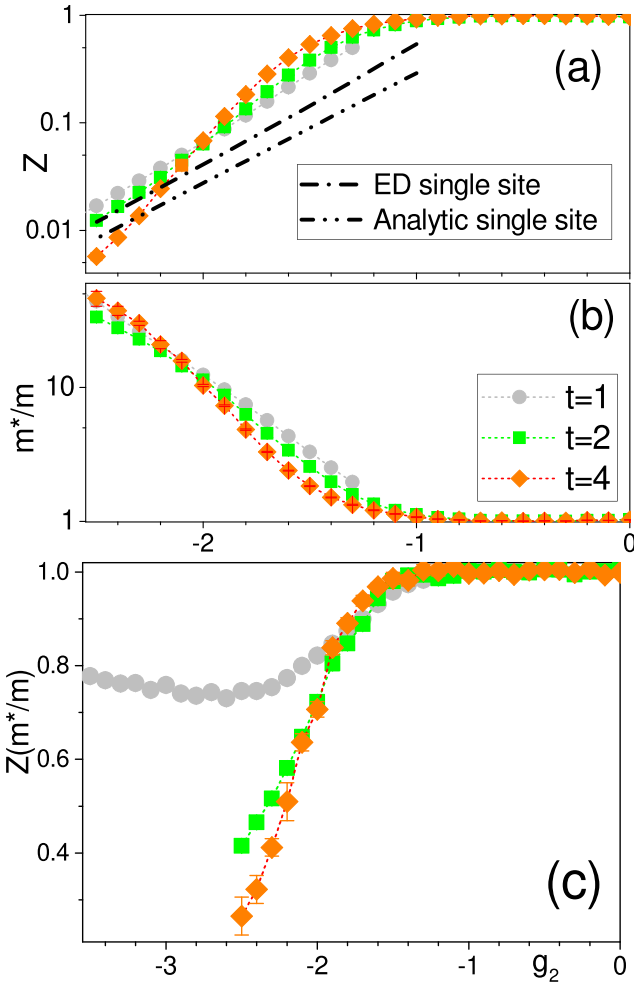

FIG. 8. Polaron properties as functions of g_2 at $\bar{\Omega} = t/2$ and $\bar{g}_4 = t/10$ for various values of γ, or, correspondingly, different values of t. The dash-dot line is the exact asymptotic behavior of Z in the single site problem obtained with ED technique. The dash-double dot line is the asymptotic analytic behavior (27).

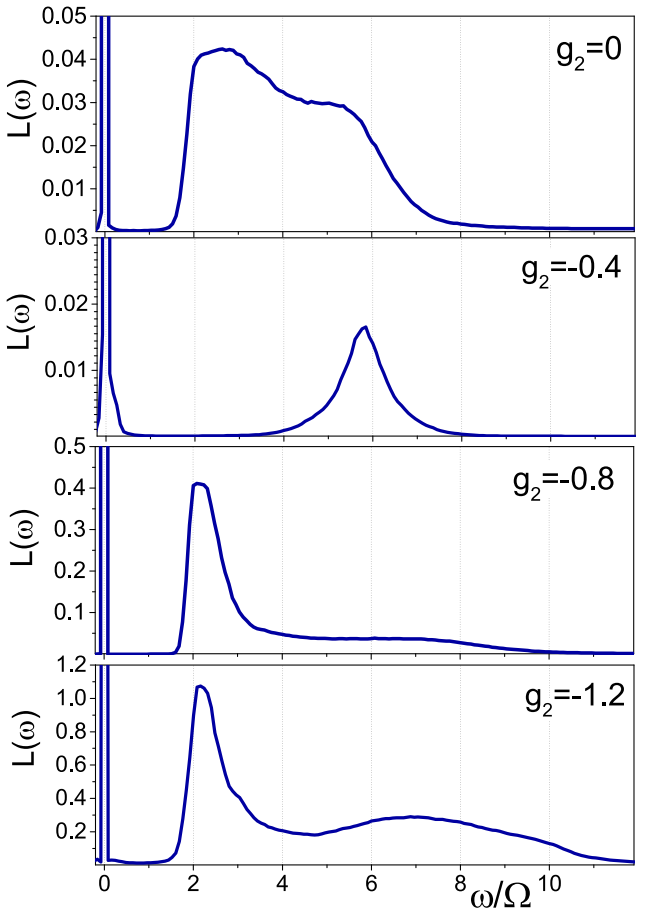

FIG. 9. Lehmann spectral function for $t = 1$, $g_4 = 0.1$, $\Omega = t/4$, and different values of g_2. Frequency is counted from the ground-state energy in units of Ω.

Finally, in the adiabatic case, starting from $\Omega/t = 1/4$, we observe that the Z factor drops below the AL prediction. This effect was never reported in the linear case. For positive quadratic coupling, $g_2 \gg 1$ and $g_4 = 0$, it signals the formation of the extended soliton (or "self-trapped") state [72]. It appears that for the double-well potential polarons can also form extended self-trapped states (finite volume with large lattice distortion moving as a whole) before reaching AL limit.

The above considerations show that the physics is reduced to a single-site problem for the asymptotically large coupling limit. Therefore, the self-energy in this regime must become local, and the relation (25) has to be valid again. This is confirmed by the behavior of $Z(m^*/m)$ at large values of $|g_2|$, namely, the upturn of the green curve in Fig. 8(c).

C. Spectral function and the structure of the phonon cloud

In this subsection, we investigate the polaron Lehmann spectral function $L(\omega)$, obtained by analytic continuation of the equation

$$G(\tau) = \int_0^\infty d\omega\, e^{-\omega\tau} L(\omega), \tag{29}$$

using the stochastic optimization with consistent constraints [73–75] method.

As intuitively expected, the spectra presented in Fig. 9 for $g_2 = 0$, $g_2 = -0.8$, and $g_2 = -1.2$ show a clear threshold for excited states at $\omega = 2\,\Omega$. Indeed, in perturbation theory, both x^2- and x^4-terms can change vibrational states only by 0, 2, 4, or any other even number of quanta. Therefore, one expects, in close analogy with well-understood linear EPI cases [28,73,76,77], that the corresponding low-energy threshold for incoherent quadratic and quartic processes is $2\,\Omega$. Moreover, since the spectral weight at $\omega = 4\,\Omega$ for $g_2 = -1.2$ is larger than that for $g_2 = -0.8$, we conclude that for our parameters the main contribution at this frequency originates from the x^2 terms at higher expansion order. Obviously, for $g_2 = 0$, the spectral continuum is entirely controlled by the x^4 terms.

Given these considerations, the structure of the Lehmann spectral function for $g_2 = -0.4$ appears to violate the rule because the low-energy threshold is observed at $4\,\Omega$. However, as already noticed in Ref. [14], for negative g_2, there is

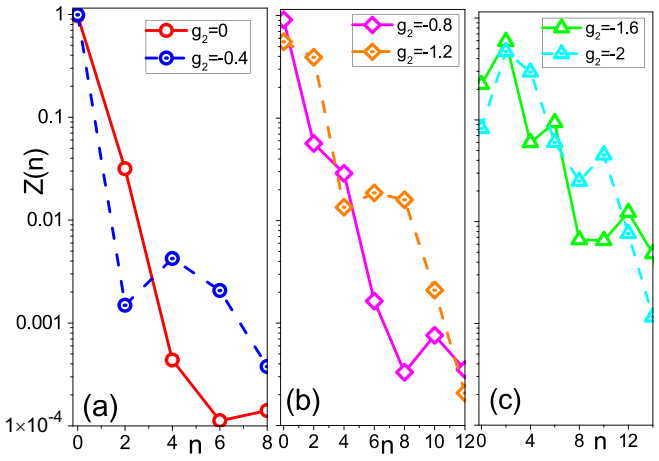

FIG. 10. Partial weights of states with a given number of phonons in the polaron cloud [$\sum_n Z(n) = 1$] for $g_4 = 0.1t$, $\Omega = t/4$, and different values of g_2.

destructive "interference" between quadratic and quartic interactions leading to the effective suppression of the total EPI strength and $Z \approx 1$. In the lowest-order perturbation theory, this destructive interference argument predicts that the spectral weight goes to 0 at $\omega = 2\,\Omega$ for $g_2 = -6g_4$, or $g_2 = -0.6t$ for $g_4 = 0.1t$ considered here. Due to the strong competition between g_2 and g_4, we name this specific scenario as *quantum interplay* regime.

A more precise treatment of the observed behavior is provided by ED studies of the partial weights $Z(n)$ of states with n phonons in the exact solution. We find that the weight of two-phonon states is significantly suppressed at $g_2 = -0.4$ [see Fig. 10(a)] to such a degree that the numerical analytic continuation can not resolve it. The other interesting feature of the phonon cloud structure, which has never been observed before in systems with nonlinear EPI, is the oscillatory dependence of $Z(n)$ on n and g_2 at large coupling $|g_2| > 1$ [see Figs. 10(b) and 10(c)].

IV. CONCLUSIONS

In this work, we developed the numeric X-propagator technique for accurately solving a broad class of polaron models without approximations. This approach can treat (1) arbitrary coupling of the intersite hopping amplitude magnitude to the local coordinates of atoms on sites i, j, and the bond $\langle ij \rangle$ between them, i.e., $t_{ij}(x_i, x_j, x_{ij}) = t \exp\{S(x_i, x_j, x_{ij})\}$ with an arbitrary nonpathological function S [41] and (2) arbitrary coupling between the carrier density and the on-site atomic vibration: $n_i V_{\rm ep}(x_i)$. The method itself is a hybrid of the precise numeric tabulation of the atomic coordinate X-propagator in imaginary time (either by Feynman path-integral or exact diagonalization techniques) with the lattice path integral for a single electron. The latter is "dressed" by the X propagators and simulated by the Diagrammatic Monte Carlo technique. An approximation-free solution for the electron Green's function in imaginary time allows one to obtain unbiased values for the polaron ground-state energy, quasiparticle weight, and effective mass. Numeric analytic continuation of the Green's function provides access to the Lehmann spectral function and properties of excited polaron states, which are measurable through angle-resolved photoemission experiments.

As an application, we studied a particular case of the double-well potential coupling, which is considered prototypical for several classes of materials. We compared our results to earlier studies [14,15] of the same model within the momentum average approximation framework. We find that for cases with relatively large phonon frequency, $\Omega \geqslant t/2$, this approximation provides a reasonable description of the polaron energy and quasiparticle weight, but the key property of the momentum average approximation, $(m^*/m)Z \equiv 1$, fails. The exact diagonalization technique provides a more accurate description in the same parameter range. However, both momentum average and exact diagonalization methods start to fail in the adiabatic regime $\Omega \leqslant t/4$, leaving our technique as the only unbiased approach suitable for dealing with realistic materials. We extended our calculations to the deep adiabatic regime $\Omega = t/16$, where the phonon frequency is almost two orders of magnitude smaller than the electron bandwidth.

Given that the simplest possible double-well model has four parameters, and its properties depend on three dimensionless ratios, we fixed the quartic coupling $g_4 > 0$ and investigated system properties for different adiabatic ratios Ω/t as functions of quadratic coupling g_2. We identified three qualitatively different parameter regimes: (1) The quantum interplay regime, $-g_2 \sim 4g_4$, where quadratic and quartic terms compete and the separation between the two minima of the potential $V(x)$ on the occupied site is comparable to the ionic zero-point vibration. In this regime, the destructive interference between quadratic and quartic terms may result in near complete suppression of the effective electron-phonon interaction, leading to $Z \approx 1$, $m^*/m \approx 1$, and even to the disappearance of the spectral continuum threshold at excited energy $2\,\Omega$. (2) The moderately strong coupling regime, $-g_2 < 4g_4$, in which the quasiparticle weight and effective mass are described by exponential laws $Z \propto \exp[\xi_Z g_2 \Omega^{-1/4}]$ and $m^*/m \propto \exp[-\xi_m g_2 \Omega^{-1/4}]$. We note that this regime is reached at smaller absolute values of g_2 for smaller values of Ω. (3) An extreme strong coupling regime at very large, $|g_2| > 100\,|g_4|$, values of the quadratic coupling constant. This regime corresponds to the asymptotic single-site double-well state, with exponentially small Z and m/m^*, and which is reached only at very large, $|g_2| > 100\,|g_4|$, values of the quadratic coupling constant. It is obvious, and it also follows from Fig. 8(c), that single-site physics is reached faster at larger phonon frequencies Ω due to the reduced influence of the kinetic energy of electrons caused by hopping t.

Although it seems surprising, we note that there is nothing singular in the properties of the polaron when g_2 is approaching $-\Omega/4$ from above. This absence of singularity seems counterintuitive because, when stabilizing effects of $g_4 > 0$ are missing, $g_2 = -\Omega/4$ would lead to instability of the phonon spectrum. However, the instability of the polaron on the site occupied by the electron occurs only if the electron never leaves the site, which is not the case for finite hopping. As a result, there are no singular polaron behaviors in the purely quadratic interaction model [40]. With any finite electron dispersion, the quasiparticle factor Z and the effective

mass m^*/m remain finite due to the kinetic energy driven by electron hopping [40].

Recent studies have shown that the quadratic electron-phonon coupling can lead to an increase in the superconductivity temperature T_c when only quadratic interaction is present [78,79] or when added to a system with weak linear interaction [78]. The maximal ratio T_c/Ω is reached when the renormalized phonon frequency at large positive $g_2 > 0$ becomes comparable with the electron bandwidth [79]. Actually, an increase in $g_4 > 0$ can also lead to a substantial enhancement of the phonon frequency, and one can speculate that quartic coupling can also lead to an increase in T_c/Ω. However, these observations need to be confirmed by accurate calculations that can be performed using the numerical X-propagator technique presented here, generalized to bipolarons using the approach employed in Ref. [79].

In this work, we have shown that the newly introduced numeric X-propagators technique is able to accurately solve a polaron model that features strongly anharmonic potentials that exhibit a double-well structure. This is one of the main ingredients required to investigate charge transport at low-doping concentrations in quantum paraelectric and ferroelectric materials such as $SrTiO_3$ and $BaTiO_3$. This work lays the foundation for future studies with material-specific potential profiles obtained from *ab-initio* calculations.

Moreover, it is important to emphasize that the numerical X-propagator technique is not restricted to the case of dispersionless phonons considered in this study. Indeed, a straightforward generalization of this method to the case of dispersive phonons is possible, making our approach a fundamental tool for approximation-free studies of transport and optical properties [38,39] in a wide range of realistic materials. In particular, the rigorous treatment of strong phonon dispersion becomes especially essential for quantum paraelectric and ferroelectric materials, halide perovskites, and anharmonic superconductors [80], where the phonon dispersion considerably exceeds the minimal phonon frequency [81].

ACKNOWLEDGMENTS

This work was supported in part by the Croatian Science Foundation (HRZZ) under Projects No. IP-2024-05-2406, No. IP-2022-10-9423, and No. IP-2022-10-3382. This research was funded in part by the Austrian Science Fund (FWF) 10.55776/I4506 and 10.55776/PIN5456724. For the purpose of open access, the author has applied a CC BY public copyright license to any Author Accepted Manuscript version arising from this submission. T.M. acknowledges support of the project FrustKor financed by the EU through the National Recovery and Resilience Plan 2021-2026 (NRPP). O.S.B. acknowledges the support of the project "Implementation of cutting-edge research and its application as part of the Scientific Center of Excellence for Quantum and Complex Systems, and Representations of Lie Algebras," Grant No. PK.1.1.10.0004, co-financed by the European Union through the European Regional Development Fund—Competitiveness and Cohesion Programme 2021–2027. N.P. acknowledges support from the National Science Foundation under Grant No. DMR-2335904. N.N. was supported by JSPS KAKENHI Grants No. 24H00197, No. 24H02231, No. 24K00583, and by the RIKEN TRIP initiative. Most computations were carried out on the Vienna Scientific Cluster (VSC) and the computational facilities of RIKEN Center for Emergent Matter Science (CEMS).

DATA AVAILABILITY

The data that support the findings of this article are openly available [82].

APPENDIX A: CALCULATION OF THE OSCILLATOR PROPAGATOR WITH ARBITRARY ELECTRON-PHONON POTENTIAL BY TROTTER-SUZUKI DECOMPOSITION

This Appendix describes the method of calculation of the X propagator in the case of a general electron-phonon potential $V_{\rm ep}(X)$ which, in contrast to the SSED method, does not require the representation of the interaction potential in the form (2) or (5).

The propagator (6) can be presented as a path integral

$$\tilde{U}(x(\tau_f), x(\tau_i), \tau_f - \tau_i) = A(\tau)\, e^{\Omega\tau/2} \int_{\text{all paths}} \exp\left\{-\int_{\tau_i}^{\tau_f}\left[\frac{1}{2}(\partial x/\partial\tau)^2 + V(x)\right]\right\}, \tag{A1}$$

where $A(\tau)$ is a normalization constant. The exponent $e^{\Omega\tau/2}$ is added to provide τ-independent asymptotic behavior for $\tau \to \infty$.

1. Analytic expressions for specific potentials

The explicit form of the X propagator is known when $V_{\rm ep}(x) = 0$. It reads [83]

$$U(x, y, \tau) = \sqrt{\frac{\Omega}{2\pi \sinh[\Omega\tau]}}\, e^{\frac{1}{2}\Omega\tau - Q(x,y,\tau)}, \tag{A2}$$

where

$$Q(x, y, \tau) = \Omega\frac{\cosh[\Omega\tau](x^2 + y^2) - 2xy}{2\sinh[\Omega\tau]}. \tag{A3}$$

An important property of the X propagator is the limiting behavior

$$U(x, y, \tau \to \infty) = U_0(x)U_0(y), \tag{A4}$$

where

$$U_0(x) = (\Omega/\pi)^{1/4} e^{-\Omega x^2/2}. \tag{A5}$$

Also, when the expansion of $V_{\rm ep}(x)$ is limited to linear ($g_1 \neq 0$) and quadratic ($g_2 \neq 0$) terms, one can transfer the potential (4) to

$$V(x) = \frac{\Omega_{\rm at}^2}{2}(x + \xi_{\rm sh})^2 + \Delta_{\rm sh} + \frac{\Omega_{\rm at}}{2}, \tag{A6}$$

where

$$\Omega_{\rm at} = \Omega\sqrt{1 + n\frac{4g_2}{\Omega}}, \tag{A7}$$

$$\xi_{\rm sh} = \frac{g_1}{\Omega_{\rm at}^2}\sqrt{2\Omega}, \tag{A8}$$

and

$$\Delta_{\rm sh} = -\frac{g_1^2}{\Omega_{\rm at}^2}\Omega. \tag{A9}$$

In this case, the X propagator is

$$\tilde{\mathbf{U}}(x, y, \tau) = \sqrt{\frac{\Omega_{\rm at}}{2\pi \sinh[\Omega_{\rm at}\tau]}} e^{\frac{1}{2}\Omega\tau - \tilde{Q}(x,y,\tau) + \Delta_{\rm sh}}, \tag{A10}$$

where

$$\tilde{Q}(x, y, \tau) = \Omega_{\rm at}\frac{\cosh[\Omega_{\rm at}\tau](\bar{x}^2 + \bar{y}^2) - 2\bar{x}\bar{y}}{2\sinh[\Omega_{\rm at}\tau]} \tag{A11}$$

and

$$\bar{x} = x + \xi_{\rm sh},\ \bar{y} = y + \xi_{\rm sh}. \tag{A12}$$

Thus, if an arbitrary potential $V(x)$ on the (x, x') interval is Taylor expanded around point $\bar{x} = (x + x')/2$:

$$V(x) \approx V(\bar{x}) + V'(\bar{x})(x - \bar{x}) + V''(\bar{x})(x - \bar{x})^2/2, \tag{A13}$$

one can use Eqs. (A10)–(A12) to obtain the most accurate analytic solution for the propagator $P(x, x', \delta\tau)$.

2. Path-integral representation for an arbitrary potential: Monte Carlo updates

For a concise description of updates, let us represent the propagator between any left i and right $i + 1$ points (21) as

$$P(x_i, x_{i+1}, \delta\tau) = \exp\{-\Theta[x_i, x_{i+1}]\}. \tag{A14}$$

Then, four updates will ensure ergodic sampling of the configuration space: changing x_i at intermediate points, changing initial (final) x_i (x_f) coordinates, adding and removing one slice at the end.

3. Updates

a. Intermediate point update

In this case, we chose any intermediate time slice i and propose to change x_i to $x_i \pm z$ by selecting z from the exponential distribution

$$W(z) = \kappa e^{-\kappa z}, \tag{A15}$$

where κ is uniformly seeded in the range $1/\Omega m < \kappa < m/\Omega$ with $m \approx 3$. The Metropolis algorithm ratio is

$$r = \exp\{-\theta[x_{i-1}, x_i \pm z] - \theta[x_i \pm z, x_{i+1}] + \theta[x_{i-1}, x_i] + \theta[x_i, x_{i+1}]\}. \tag{A16}$$

b. Initial (final) point update

Now, we select either the initial or final point and propose to update its oscillator coordinates by exactly the same protocol as for intermediate points. The Metropolis ratio is now (for final point)

$$r = \exp\{-\theta[x_{f-1}, x_f \pm z] + \theta[x_{f-1}, x_f]\}. \tag{A17}$$

c. Adding (removing) slice update

We propose to add one slice at the end with $x_{f+1} = x_f$. Again, we generate z from Eq. (A15) and propose to change x_f to $x_f \pm z$. The Metropolis ratio is now

$$r = \frac{\exp\{-\theta[x_{f-1}, x_f \pm z] - \theta[x_f \pm z, x_f] + \theta[x_{f-1}, x_f]\}}{(\kappa/2)\exp(-\kappa z)}. \tag{A18}$$

In the removal case, the ratio is the reciprocal.

APPENDIX B: CALCULATION OF THE OSCILLATOR PROPAGATOR BY SSED

Consider Eq. (2) at a single site

$$\hat{H} = \Omega\,\hat{b}^\dagger\hat{b} + \sum_{i=1,2,4} g_i(\hat{b} + \hat{b}^\dagger)^i. \tag{B1}$$

Its matrix elements in the phonon number basis are straightforwardly calculated. For $m \geqslant n$,

$$\langle m|\,\hat{H}_1\,|n\rangle = g_1 \cdot \delta(m, n-1) \cdot \sqrt{n}, \tag{B2}$$

$$\langle m|\,\hat{H}_2\,|n\rangle = g_2 \cdot (\delta(m, n-2) \cdot \sqrt{n(n-1)} + \delta(m, n) \cdot (1 + 2n)), \tag{B3}$$

$$\langle m|\,\hat{H}_4\,|n\rangle = g_4 \cdot (\delta(m, n-4) \cdot \sqrt{n(n-1)(n-2)(n-3)} + \delta(m, n-2) \cdot 2(2n-1)\sqrt{n(n-1)} + \delta(m, n) \cdot 3(2n^2 + 2n + 1)). \tag{B4}$$

This matrix is real and symmetric, so it can be diagonalized with real eigenvalues and eigenvectors. The energy eigenstates can be labeled by a discrete quantum number ξ. The complete basis is composed of an infinite number of them, $\{|\xi\rangle\}_{\xi=0}^{\infty}$. In order to perform the diagonalization with a computer, we must impose an upper cutoff in the number of phonon states that we consider. When this cutoff is made large enough, we recover the exact eigenstates.

The propagator may then be expressed in terms of the eigenvalues and eigenvectors resulting from the diagonalization

$$U(y, x, \tau) \equiv \langle y|\,e^{-\tau\hat{H}}\,|x\rangle \tag{B5}$$

$$= \sum_{\xi} \langle y|\xi\rangle\,\langle\xi\,|x\rangle\,e^{-\tau E_\xi} \tag{B6}$$

$$= \sum_{\xi}\sum_{m,n} \langle y|n\rangle\,\langle n|\xi\rangle\,\langle\xi\,|m\rangle\,\langle m|x\rangle\,e^{-\tau E_\xi}, \tag{B7}$$

where $\langle y|n\rangle$ is the Hermite function $\psi_n(y)$ and $\langle m|x\rangle$ is the complex conjugate of the Hermite function $\psi_m(x)$. Because Hermite functions are real, $\psi_m^*(x) = \psi_m(x)$. $\langle n|\xi\rangle$ and $\langle\xi\,|m\rangle$ are the expansion coefficients of the eigenvectors of $\hat{H}$ in the phonon number basis. Since the eigenvectors are real, $\langle\xi\,|m\rangle = \langle m|\xi\rangle$. E_ξ are the eigenvalues obtained by the diagonalization of $\hat{H}$.

The evaluation of the quantity in Eq. (B7) is too expensive to be performed at each Monte Carlo step. For this reason, the propagator is precomputed in advance at a dense grid of points, and continuous values in between are obtained by linear interpolation.

The single-site Green's Function (18) is expressed in terms of Eqs. (B5) and (A5):

$$G^0(\tau) = \int_{-\infty}^{\infty} \mathrm{d}y \int_{-\infty}^{\infty} \mathrm{d}x\, U_0(y) U(y, x, \tau) U_0(x). \tag{B8}$$

By the orthonormality of the Hermite polynomials $H_n(x)$ to the constant function 1,

$$\int_{-\infty}^{\infty} \mathrm{d}x\, e^{-\Omega x^2} H_n(\sqrt{\Omega} x) = \sqrt{\frac{\pi}{\Omega}}\, \delta_{n=0}, \tag{B9}$$

one obtains

$$G^0(\tau) = \sum_{\xi} \langle 0|\xi\rangle^2\, e^{-\tau E_\xi}, \tag{B10}$$

so that $Z_0^{\mathrm{AL}} = \langle 0|\xi\rangle^2$.

The SSED method has the advantage that we obtain with great precision many quantities useful for the Monte Carlo process. One is the τ derivative of Eq. (B7), which enters the energy estimator that will be described in the next Appendix. Another is the integral of $G_0(\tau)$, which allows us to get the correct normalization for the measurement of the Green's function. The collected histogram is multiplied by the normalization constant

$$C = \frac{N}{N_0} I_0, \quad I_0 = \int_0^{\tau_{\max}} \mathrm{d}\tau\, G^0(\tau), \tag{B11}$$

where N_0/N is the statistics of the zeroth order diagram, and I_0 is obtained by integrating Eq. (B10) term by term. This normalization method ensures better statistics than the simpler method employing the property $G(\tau = 0) = 1$ and removes its systematic error due to the size of the τ bin.

Another advantage of this method over the path integral one is the possibility of obtaining the propagator for a nonuniform grid in imaginary time, better suited for the region of small imaginary times where the Green's function changes rapidly.

APPENDIX C: DIRECT ESTIMATORS FOR THE ENERGY AND THE EFFECTIVE MASS

Alongside with the usual method which extracts ground-state properties from the Green's function, we derive direct estimators for the energy and effective mass.

Both derivations follow the same strategy: equating the Green's function in the asymptotic τ limit

$$G(k, \tau \to \infty) \to Z_0(k) e^{-E_0(k)\tau} = e^{-E_0(k)\tau + \ln(Z_0(k))} \tag{C1}$$

to its general expression, transformed to position space and expanded into the perturbation series

$$G(\Delta r, \tau) = \sum_{\nu} W_\nu(\Delta r, \tau), \tag{C2}$$

where $\nu \equiv (n, \{\tau_i\}, \{x_j\})$ is a collective coordinate that includes all summation indices and integration variables of the diagram: order n (number of hoppings), imaginary times $\{\tau_i\}$, and displacements $\{x_j\}$, and W_ν is the diagram weight.

1. Energy estimator

On one hand, taking the logarithmic derivative with respect to τ of (C1)

$$\frac{1}{G(k,\tau)} \frac{\mathrm{d}G(k,\tau)}{\mathrm{d}t} = -E_0(k). \tag{C3}$$

On the other hand, using the perturbation expansion (C2)

$$\begin{aligned} \frac{1}{G(k,\tau)} \frac{\mathrm{d}G(k,\tau)}{\mathrm{d}t} &= \frac{\sum_{\Delta r} e^{-ik\Delta r} \frac{\mathrm{d}G(\Delta r,\tau)}{\mathrm{d}t}}{\sum_{\Delta r} e^{-ik\Delta r} G(\Delta r, \tau)} \\ &= \frac{\sum_{\Delta r,\nu} e^{-ik\Delta r} W_\nu(\Delta r,\tau) \frac{1}{W_\nu(\Delta r,\tau)} \frac{\mathrm{d}W_\nu(\Delta r,\tau)}{\mathrm{d}t}}{\sum_{\Delta r,\nu} e^{-ik\Delta r} W_\nu(\Delta r,\tau)} \\ &= \frac{\left\langle e^{-ik\Delta r} \frac{1}{W_\nu(\Delta r,\tau)} \frac{\mathrm{d}W_\nu(\Delta r,\tau)}{\mathrm{d}t} \right\rangle_{\mathrm{MC}}}{\langle e^{-ik\Delta r}\rangle_{\mathrm{MC}}}. \end{aligned} \tag{C4}$$

In order to take the τ derivative of the diagram weight W, one must make explicit the dependence on τ of the internal times τ_i:

$$\tau_i' \equiv \tau_i/\tau, \quad \tau_i = \tau\, \tau_i'. \tag{C5}$$

Due to the change of integration variables $\tau_i \to \tau_i'$, $\mathrm{d}\tau_i = \tau \mathrm{d}\tau_i'$ so the diagram weight becomes

$$W_{\nu'}(\Delta r, \tau) = \tau^n W_\nu(\Delta r, \tau), \quad \nu' \equiv (n, \{\tau_i'\}, \{x_j\}), \tag{C6}$$

$$\frac{\mathrm{d}\ln W_{\nu'}(\Delta r,\tau)}{\mathrm{d}\tau} = \frac{1}{\tau}\left(n + \sum_i \frac{\mathrm{d}\ln U(y_i, x_i, \tau_i)}{\mathrm{d}\tau_i}\, \tau_i\right). \tag{C7}$$

The final result for the energy estimator is

$$E_0(k) = \frac{\left\langle e^{-ik\Delta r} \frac{1}{\tau}\left(-n - \sum_i \frac{\mathrm{d}\ln U(y_i,x_i,\tau_i)}{\mathrm{d}\tau_i}\, \tau_i\right)\right\rangle_{\mathrm{MC}}}{\langle e^{-ik\Delta r}\rangle_{\mathrm{MC}}}. \tag{C8}$$

2. Effective mass estimator

On one hand, taking the second log-derivative of (C1) with respect to k at $k = 0$,

$$\frac{1}{G(k,\tau)} \frac{\mathrm{d}^2 G(k,\tau)}{\mathrm{d}k^2}_{k=0} = -\frac{\tau}{m^*} + \frac{\mathrm{d}^2 \ln(Z)}{\mathrm{d}k^2}_{k=0}, \tag{C9}$$

where we used the fact that the first derivative of $Z(k)$ vanishes at $k = 0$ because $Z(k)$ is an even function, and

$$\frac{1}{m^*} = \frac{\mathrm{d}^2 E_0}{\mathrm{d}k^2}_{k=0}. \tag{C10}$$

On the other hand, one can transform the Green's function to position space

$$G(k,\tau) = \sum_{\Delta r} e^{-ik\Delta r} G(\Delta r, \tau). \tag{C11}$$

Now, we take the second log-derivative in k of Eq. (C11), and then substitute the expression (C2)

$$\begin{aligned} \frac{1}{G(k,\tau)} \frac{\mathrm{d}^2 G(k,\tau)}{\mathrm{d}k^2}_{k=0} &= \frac{\sum_{\Delta r} -(\Delta r)^2 G(\Delta r,\tau)}{\sum_{\Delta r} G(\Delta r,\tau)} \\ &= \frac{\sum_{\Delta r,\nu} -(\Delta r)^2 W_\nu(\Delta r,\tau)}{\sum_{\Delta r,\nu} W_\nu(\Delta r,\tau)} \\ &= \langle -(\Delta r)^2\rangle_{\mathrm{MC}}. \end{aligned} \tag{C12}$$

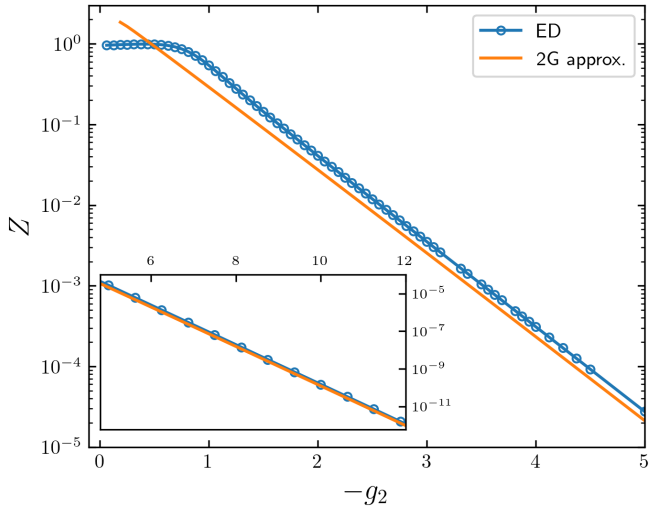

FIG. 11. Comparison between analytical formula (27) labeled 2G (double-Gaussian) approximation, and the result from single-site ED, for $g_4 = 0.1$ and $\Omega = 0.5$. Even at $g_2 = -12$, the error is 17%.

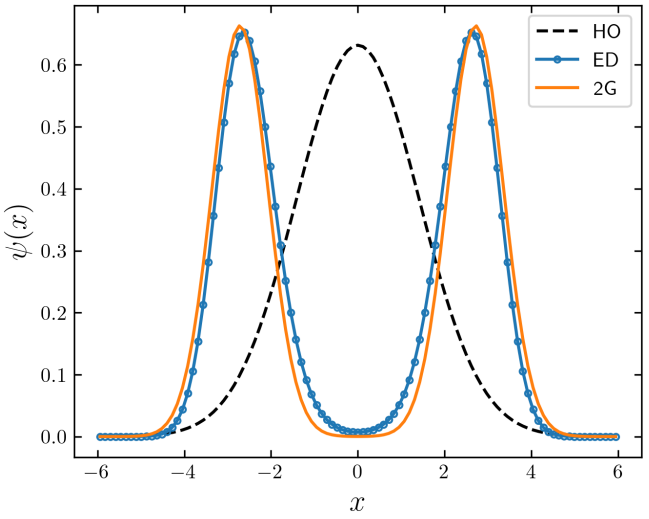

FIG. 12. Comparison between the double-Gaussian (2G) approximation (D2) to the wavefunction at $g_2 = -1.6$ and the single-site ED result. The HO ground state (D1) is also shown for reference.

By equating Eqs. (C9) and Eq. (C12), we arrive at the final expression for the effective mass estimator

$$\frac{1}{m^*} - \frac{1}{\tau}\frac{\mathrm{d}^2 \ln(Z)}{\mathrm{d}k^2}\bigg|_{k=0} = \left\langle \frac{(\Delta r)^2}{\tau} \right\rangle_{\mathrm{MC}}. \tag{C13}$$

The simulation is obviously restricted to a finite $\tau_{\max}$, while we need to extrapolate to $\tau \to \infty$ to obtain $1/m^*$. Thus, we perform a linear fit of the MC estimator versus $1/\tau$ and take the intercept as our unbiased value of the inverse effective mass.

APPENDIX D: ANALYTICAL FORMULA FOR ASYMPTOTIC VALUE OF Z FACTOR AT LARGE $|g_2|$

When $|g_2|$ is large, the two wells become deep and separated so that the oscillator's wave function can be approximated with a superposition of harmonic states centered in the double well's minima $\pm x_0$ (7) and with renormalized frequency $\tilde{\omega}$ (9)

$$\psi_0(x) = \left(\frac{\Omega}{\pi}\right)^{1/4} \exp\left(-\frac{\Omega x^2}{2}\right), \tag{D1}$$

$$\tilde{\psi}_0(x) = \frac{\psi_+ + \psi_-}{\sqrt{2}}, \tag{D2}$$

$$\tilde{\psi}_\pm(x) = \left(\frac{\tilde{\omega}}{\pi}\right)^{1/4} \exp\left(-\frac{\tilde{\omega}(x \mp x_0)^2}{2}\right). \tag{D3}$$

Note that this calculation assumes a single-site system ($t = 0$) or a system where $t \ll |g_2|$.

Computing the overlap

$$\langle \psi_0 | \tilde{\psi}_+ \rangle = \left(\frac{\Omega\tilde{\omega}}{\pi^2}\right)^{1/4} \int \mathrm{d}x\, e^{-\Omega x^2/2}\, e^{-\tilde{\omega}(x-x_0)^2/2} \tag{D4}$$

$$= \left(\frac{R}{\pi^2}\right)^{1/4} \int \mathrm{d}z\, \exp\left(-\frac{z^2}{2} - \frac{R(z-z_0)^2}{2}\right) \tag{D5}$$

$$= \left(\frac{R}{\pi^2}\right)^{1/4} \sqrt{\frac{2\pi}{1+R}} \exp\left(-\frac{R}{1+R} z_0^2\right), \tag{D6}$$

one gets Z factor $Z = \langle \psi_0 | \tilde{\psi}_0 \rangle^2$, which results in the final expression (27).

Figure 11 shows that the asymptotic formula is valid only at very large values of $|g_2|$. To better understand the reason for the discrepancy, in Fig. 12, we plot the wavefunctions (D1) and (D2) used to obtain the Z factor, at an intermediate value of the coupling $g_2 = -1.6$. Near $x = 0$, where the ground-state wavefunction of the harmonic oscillator is large, the double-Gaussian wavefunction is excessively suppressed, unlike the exact wavefunction obtained through single-site ED.

[1] J. Appel, in *Polarons*, edited by F. Seitz, D. Turnbull, and H. Ehrenreich, Solid State Physics, Vol. 21, (Academic Press, New York, 1968), pp. 193–391.

[2] *Polarons in Advanced Materials*, edited by A. S. Alexandrov, Springer Series in Materials Science, Vol. 103 (Springer, Dordrecht, 2007).

[3] O. Gunnarsson and O. Rösch, Interplay between electron–phonon and Coulomb interactions in cuprates, J. Phys.: Condens. Matter **20**, 043201 (2008).

[4] C. Franchini, M. Reticcioli, M. Setvin, and U. Diebold, Polarons in materials, Nat. Rev. Mater. **6**, 560 (2021).

[5] M. J. Schilcher, P. J. Robinson, D. J. Abramovitch, L. Z. Tan, A. M. Rappe, D. R. Reichman, and D. A. Egger, The significance of polarons and dynamic disorder in halide perovskites, ACS Energy Lett. **6**, 2162 (2021).

[6] W. A. Saidi, S. Poncé, and B. Monserrat, Temperature dependence of the energy levels of methylammonium lead iodide perovskite from first-principles, J. Phys. Chem. Lett. **7**, 5247 (2016).

[7] M. Zacharias, G. Volonakis, F. Giustino, and J. Even, Anharmonic electron-phonon coupling in ultrasoft and locally disordered perovskites, npj Comput. Mater. **9**, 153 (2023).

[8] V. Esposito, M. Fechner, R. Mankowsky, H. Lemke, M. Chollet, J. M. Glownia, M. Nakamura, M. Kawasaki, Y. Tokura, U. Staub, P. Beaud, and M. Först, Nonlinear electron-phonon coupling in doped manganites, Phys. Rev. Lett. **118**, 247601 (2017).

[9] M. Hoesch, P. Piekarz, A. Bosak, M. Le Tacon, M. Krisch, A. Kozłowski, A. M. Oleś, and K. Parlinski, Anharmonicity due to electron-phonon coupling in magnetite, Phys. Rev. Lett. **110**, 207204 (2013).

[10] R. Migoni, H. Bilz, and D. Bäuerle, Origin of Raman scattering and ferroelectricity in oxidic perovskites, Phys. Rev. Lett. **37**, 1155 (1976).

[11] A. Kumar, V. I. Yudson, and D. L. Maslov, Quasiparticle and nonquasiparticle transport in doped quantum paraelectrics, Phys. Rev. Lett. **126**, 076601 (2021).

[12] S. Stemmer and S. J. Allen, Non-Fermi liquids in oxide heterostructures, Rep. Prog. Phys. **81**, 062502 (2018).

[13] L. Ranalli, C. Verdi, M. Zacharias, J. Even, F. Giustino, and C. Franchini, Electron mobilities in $SrTiO_3$ and $KTaO_3$: Role of phonon anharmonicity, mass renormalization, and disorder, Phys. Rev. Mater. **8**, 104603 (2024).

[14] C. P. J. Adolphs and M. Berciu, Single-polaron properties for double-well electron-phonon coupling, Phys. Rev. B **89**, 035122 (2014).

[15] C. P. J. Adolphs and M. Berciu, Strongly bound yet light bipolarons for double-well electron-phonon coupling, Phys. Rev. B **90**, 085149 (2014).

[16] K. L. Ngai, Two-phonon deformation potential and superconductivity in degenerate semiconductors, Phys. Rev. Lett. **32**, 215 (1974).

[17] D. E. Kiselov and M. V. Feigel'man, Theory of superconductivity due to Ngai's mechanism in lightly doped $SrTiO_3$, Phys. Rev. B **104**, L220506 (2021).

[18] P. A. Volkov, P. Chandra, and P. Coleman, Superconductivity from energy fluctuations in dilute quantum critical polar metals, Nat. Commun. **13**, 4599 (2022).

[19] A. Bussmann-Holder, A. Simon, and H. Büttner, Possibility of a common origin to ferroelectricity and superconductivity in oxides, Phys. Rev. B **39**, 207 (1989).

[20] T. Esswein and N. A. Spaldin, Ferroelectric, quantum paraelectric, or paraelectric? Calculating the evolution from $BaTiO_3$ to $SrTiO_3$ to $KTaO_3$ using a single-particle quantum mechanical description of the ions, Phys. Rev. Res. **4**, 033020 (2022).

[21] L. Ranalli, C. Verdi, L. Monacelli, G. Kresse, M. Calandra, and C. Franchini, Temperature-dependent anharmonic phonons in quantum paraelectric $KTaO_3$ by first principles and machine-learned force fields, Adv. Quantum Technol. **6**, 2200131 (2023).

[22] C. Verdi, L. Ranalli, C. Franchini, and G. Kresse, Quantum paraelectricity and structural phase transitions in strontium titanate beyond density functional theory, Phys. Rev. Mater. **7**, L030801 (2023).

[23] M. Houtput, L. Ranalli, C. Verdi, S. Klimin, S. Ragni, C. Franchini, and J. Tempere, First-principles theory of nonlinear long-range electron-phonon interaction, Phys. Rev. B **111**, 184320 (2025).

[24] R. Bianco and I. Errea, Non-perturbative theory of the electron-phonon coupling and its first-principles implementation, arXiv:2303.02621.

[25] C. P. J. Adolphs and M. Berciu, Going beyond the linear approximation in describing electron-phonon coupling: Relevance for the Holstein model, Europhys. Lett. **102**, 47003 (2013).

[26] M. Berciu, Green's function of a dressed particle, Phys. Rev. Lett. **97**, 036402 (2006).

[27] M. Berciu and G. L. Goodvin, Systematic improvement of the momentum average approximation for the Green's function of a Holstein polaron, Phys. Rev. B **76**, 165109 (2007).

[28] G. L. Goodvin, A. S. Mishchenko, and M. Berciu, Optical conductivity of the Holstein polaron, Phys. Rev. Lett. **107**, 076403 (2011).

[29] A. Kuklov, Soliton-like excitations in strongly anharmonic media, Phys. Lett. A **139**, 270 (1989).

[30] G. Paleari, F. Hébert, B. Cohen-Stead, K. Barros, R. T. Scalettar, and G. G. Batrouni, Quantum Monte Carlo study of an anharmonic Holstein model, Phys. Rev. B **103**, 195117 (2021).

[31] S. Li and S. Johnston, The effects of non-linear electron-phonon interactions on superconductivity and charge-density-wave correlations, Europhys. Lett. **109**, 27007 (2015).

[32] S. Li, E. A. Nowadnick, and S. Johnston, Quasiparticle properties of the nonlinear Holstein model at finite doping and temperature, Phys. Rev. B **92**, 064301 (2015).

[33] P. M. Dee, J. Coulter, K. G. Kleiner, and S. Johnston, Relative importance of nonlinear electron-phonon coupling and vertex corrections in the Holstein model, Commun. Phys. **3**, 145 (2020).

[34] P. S. Riseborough, The small polaron with nonlinear electron-phonon interactions, Ann. Phys. **153**, 1 (1984).

[35] M. Houtput and J. Tempere, Beyond the Fröhlich Hamiltonian: Path-integral treatment of large polarons in anharmonic solids, Phys. Rev. B **103**, 184306 (2021).

[36] S. N. Klimin, J. Tempere, M. Houtput, S. Ragni, T. Hahn, C. Franchini, and A. S. Mishchenko, Analytic method for quadratic polarons in nonparabolic bands, Phys. Rev. B **110**, 075107 (2024).

[37] R. P. Feynman, Slow electrons in a polar crystal, Phys. Rev. **97**, 660 (1955).

[38] A. S. Mishchenko, N. Nagaosa, G. De Filippis, A. de Candia, and V. Cataudella, Mobility of Holstein polaron at finite temperature: An unbiased approach, Phys. Rev. Lett. **114**, 146401 (2015).

[39] A. S. Mishchenko, L. Pollet, N. V. Prokof'ev, A. Kumar, D. L. Maslov, and N. Nagaosa, Polaron mobility in the "beyond quasiparticles" regime, Phys. Rev. Lett. **123**, 076601 (2019).

[40] S. Ragni, T. Hahn, Z. Zhang, N. Prokof'ev, A. Kuklov, S. Klimin, M. Houtput, B. Svistunov, J. Tempere, N. Nagaosa, C. Franchini, and A. S. Mishchenko, Polaron with quadratic

electron-phonon interaction, Phys. Rev. B **107**, L121109 (2023).
[41] N. V. Prokof'ev and B. V. Svistunov, Phonon modulated hopping polarons: x-representation technique, Phys. Rev. B **106**, L041117 (2022).
[42] F. Kluibenschedl, G. M. Koutentakis, R. Alhyder, and M. Lemeshko, Domain-wall ferroelectric polarons in a two-dimensional rotor lattice model, Phys. Rev. Lett. **134**, 096302 (2025).
[43] D. Joseph and C. Franchini, Coupling between small polarons and ferroelectricity in $BaTiO_3$, Phys. Rev. Mater. **9**, 094415 (2025).
[44] D. Shin, S. Latini, C. Schäfer, S. A. Sato, U. De Giovannini, H. Hübener, and A. Rubio, Quantum paraelectric phase of $SrTiO_3$ from first principles, Phys. Rev. B **104**, L060103 (2021).
[45] X. He, D. Bansal, B. Winn, S. Chi, L. Boatner, and O. Delaire, Anharmonic eigenvectors and acoustic phonon disappearance in quantum paraelectric $SrTiO_3$, Phys. Rev. Lett. **124**, 145901 (2020).
[46] J.-J. Zhou and M. Bernardi, Predicting charge transport in the presence of polarons: The beyond-quasiparticle regime in $SrTiO_3$, Phys. Rev. Res. **1**, 033138 (2019).
[47] S. Barišić, J. Labbé, and J. Friedel, Tight binding and transition-metal superconductivity, Phys. Rev. Lett. **25**, 919 (1970).
[48] S. Barišić, Rigid-atom electron-phonon coupling in the tight-binding approximation. I, Phys. Rev. B **5**, 932 (1972).
[49] S. Barišić, Self-consistent electron-phonon coupling in the tight-binding approximation. II, Phys. Rev. B **5**, 941 (1972).
[50] W. P. Su, J. R. Schrieffer, and A. J. Heeger, Solitons in polyacetylene, Phys. Rev. Lett. **42**, 1698 (1979).
[51] J. Bonča, S. A. Trugman, and I. Batistić, Holstein polaron, Phys. Rev. B **60**, 1633 (1999).
[52] G. De Filippis, V. Cataudella, A. S. Mishchenko, and N. Nagaosa, Optical conductivity of polarons: Double phonon cloud concept verified by diagrammatic Monte Carlo simulations, Phys. Rev. B **85**, 094302 (2012).
[53] D. J. J. Marchand, G. De Filippis, V. Cataudella, M. Berciu, N. Nagaosa, N. V. Prokof'ev, A. S. Mishchenko, and P. C. E. Stamp, Sharp transition for single polarons in the one-dimensional Su-Schrieffer-Heeger model, Phys. Rev. Lett. **105**, 266605 (2010).
[54] C. Zhang, N. V. Prokof'ev, and B. V. Svistunov, Peierls/Su-Schrieffer-Heeger polarons in two dimensions, Phys. Rev. B **104**, 035143 (2021).
[55] I. B. Bersuker and V. Z. Polinger, *Vibronic Interactions in Molecules and Crystals* (Springer Science & Business Media, Berlin/Heidelberg, 2012), Vol. 49.
[56] D. Böuerle, D. Wagner, M. Wöhlecke, B. Dorner, and H. Kraxenberger, Soft modes in semiconducting $SrTiO_3$: II. The ferroelectric mode, Z. Phys. B **38**, 335 (1980).
[57] I. S. Tupitsyn, A. S. Mishchenko, N. Nagaosa, and N. Prokof'ev, Coulomb and electron-phonon interactions in metals, Phys. Rev. B **94**, 155145 (2016).
[58] E. G. Brovman and Y. Kagan, The phonon spectrum of metals, Zh. Eksp. Teor. Fiz. **52**, 557 (1967) [Sov. Phys. JETP **25**, 365 (1967)].
[59] A. S. Mishchenko, I. S. Tupitsyn, N. Nagaosa, and N. Prokof'ev, Fermi blockade of the strong electron–phonon interaction in modelled optimally doped high temperature superconductors, Sci. Rep. **11**, 9699 (2021).
[60] A. Macridin, G. A. Sawatzky, and M. Jarrell, Two-dimensional Hubbard-Holstein bipolaron, Phys. Rev. B **69**, 245111 (2004).
[61] A. S. Mishchenko, N. Nagaosa, A. Alvermann, H. Fehske, G. De Filippis, V. Cataudella, and O. P. Sushkov, Localization-delocalization transition of a polaron near an impurity, Phys. Rev. B **79**, 180301 (2009).
[62] H. F. Trotter, On the product of semi-groups of operators, Proc. Am. Math. Soc. **10**, 545 (1959).
[63] M. Suzuki, Generalized Trotter's formula and systematic approximants of exponential operators and inner derivations with applications to many-body problems, Commun. Math. Phys. **51**, 183 (1976).
[64] D. M. Ceperley, Path integrals in the theory of condensed helium, Rev. Mod. Phys. **67**, 279 (1995).
[65] O. S. Barišić, Holstein light quantum polarons on the one-dimensional lattice, Phys. Rev. B **73**, 214304 (2006).
[66] A. Alvermann, H. Fehske, and S. A. Trugman, Solution of the Holstein polaron anisotropy problem, Phys. Rev. B **78**, 165106 (2008).
[67] T. Hahn, N. Nagaosa, C. Franchini, and A. S. Mishchenko, Diagrammatic quantum Monte Carlo study of an acoustic lattice polaron, Phys. Rev. B **104**, L161111 (2021).
[68] Y. Toyozawa, Self-trapping of an electron by the acoustical mode of lattice vibration. I: Prog. Theor. Phys. **26**, 29 (1961).
[69] A. S. Mishchenko, N. Nagaosa, and N. Prokof'ev, Diagrammatic Monte Carlo method for many-polaron problems, Phys. Rev. Lett. **113**, 166402 (2014).
[70] P. Mitrić, V. Janković, N. Vukmirović, and D. Tanasković, Spectral functions of the Holstein polaron: Exact and approximate solutions, Phys. Rev. Lett. **129**, 096401 (2022).
[71] G. L. Goodvin and M. Berciu, Momentum average approximation for models with electron-phonon coupling dependent on the phonon momentum, Phys. Rev. B **78**, 235120 (2008).
[72] Z. Zhang, A. Kuklov, N. Prokof'ev, and B. Svistunov, Soliton states from quadratic electron-phonon interaction, Phys. Rev. B **108**, 245127 (2023).
[73] A. S. Mishchenko, N. V. Prokof'ev, A. Sakamoto, and B. V. Svistunov, Diagrammatic quantum Monte Carlo study of the Fröhlich polaron, Phys. Rev. B **62**, 6317 (2000).
[74] A. S. Mishchenko, *Stochastic Optimization Method for Analytic Continuation*, edited by E. Pavarini, E. Koch, F. Anders, and M. Jarrell, From Models to Materials Modeling and Simulation, Vol. 2, (Verlag des Forschungszentrum, Julich, 2012).
[75] O. Goulko, A. S. Mishchenko, L. Pollet, N. Prokof'ev, and B. Svistunov, Numerical analytic continuation: Answers to well-posed questions, Phys. Rev. B **95**, 014102 (2017).
[76] A. S. Mishchenko, N. Nagaosa, N. V. Prokof'ev, A. Sakamoto, and B. V. Svistunov, Optical conductivity of the Fröhlich polaron, Phys. Rev. Lett. **91**, 236401 (2003).
[77] G. De Filippis, V. Cataudella, A. S. Mishchenko, C. A. Perroni, and J. T. Devreese, Validity of the Franck-Condon principle in the optical spectroscopy: Optical conductivity of the Fröhlich polaron, Phys. Rev. Lett. **96**, 136405 (2006).
[78] Z. Han, S. A. Kivelson, and P. A. Volkov, Quantum bipolaron superconductivity from quadratic electron-phonon coupling, Phys. Rev. Lett. **132**, 226001 (2024).

[79] Z. Zhang, A. Kuklov, N. Prokof'ev, and B. Svistunov, Superconductivity of bipolarons from quadratic electron-phonon interaction, Phys. Rev. B **111**, 134504 (2025).

[80] C. Setty, M. Baggioli, and A. Zaccone, Anharmonic theory of superconductivity and its applications to emerging quantum materials, J. Phys.: Condens. Matter **36**, 173002 (2024).

[81] Y. Yamada and G. Shirane, Neutron scattering and nature of the soft optical phonon in $SrTiO_3$, J. Phys. Soc. Jpn. **26**, 396 (1969).

[82] S. Ragni, Data for "Polarons with arbitrary nonlinear electron-phonon interaction" [Data set], Zenodo (2025), doi: 10.5281/zenodo.17611045.

[83] L. Moriconi, An elementary derivation of the harmonic oscillator propagator, Am. J. Phys. **72**, 1258 (2004).